Catalysis Today 437 (2024) 114764

Contents lists available at ScienceDirect

Catalysis Today

journal homepage: www.elsevier.com/locate/cattod

Influence of the surface structure of the TiO_2 support on the properties of the Au/TiO_2 photocatalyst for water treatment under visible light

Estrella Serra-Pérez [a], Goran Dražić [a], Mai Takashima [b], Bunsho Ohtani [c], Sebastijan Kovačič [a,d], Gregor Žerjav [a,*], Nataša Novak Tušar [a,e,**]

[a] National Institute of Chemistry, Hajdrihova 19, Ljubljana SI-1000, Slovenia
[b] Graduate School of Engineering, Nagoya University, Furo-cho, Nagoya 464-8603, Japan
[c] Nonprofitable Organization touche NPO, 1-6-414, North 4, West 14, Sapporo 060-0004, Japan
[d] Faculty of Chemistry and Chemical Engineering, University of Maribor, Smetanova 17, Maribor SI-2000, Slovenia
[e] University of Nova Gorica, Vipavska 13, Nova Gorica SI-5000, Slovenia

ARTICLE INFO

Keywords:
TiO_2 nanorods
Surface charge
Amorphous surface
Au/TiO_2 composites
Reversed double-beam photoacoustic spectroscopy
Photocatalysis

ABSTRACT

Plasmonic composites combining titanium dioxide (TiO_2) with highly dispersed noble metal nanoparticles have attracted great interest as they exhibit improved photocatalytic performance compared to the bare TiO_2. In this article, TiO_2–Au composite nanorods were synthesised by wet impregnation in combination with calcination. The obtained plasmonic composites were characterized by TEM, SEM, XRD, N_2 sorption, UV-Vis diffuse reflectance spectroscopy (UV-Vis DR) and reversed double-beam photoacoustic spectroscopy (RDB-PAS) analysis. The RDB-PAS analysis revealed that the TiO_2 nanorods (TNR) contain amorphous areas on the surface that influence the size of the grown gold nanoparticles. The amount of amorphous phase on the TiO_2 surface of the analysed TNR samples increases from 16.4 %, 17 % and 20.2 % for TNR-A, TNR-B and TNR-C, respectively, and is closely related to the point of charge(pH_{PZC}), which increases from the 3.9 ± 0.06, 4.7 ± 0.07 and 5.7 ± 0.04 for TNR-A, TNR-B and TNR-C, respectively. Au nanoparticle size distribution analysis obtained on the TNR surface shows that smaller Au nanoparticles are formed with pH_{PZC} increase of the TNR support, i.e. 14.8 nm, 12.5 nm and 11.6 nm for TNR-A, TNR-B and TNR-C, respectively. This confirms that the differences in the surface charge of the TiO_2 support influence the extent of hydrolysis of the Au precursor and its subsequent nucleation. Finally, the formation of $OH^{\bullet}$ radicals was monitored using fluorescence probe method with coumarin as the probe molecule. The results revealed that the TiO_2/Au composites are capable of generating $OH^{\bullet}$ radicals under visible light illumination, with cat-C, containing the smallest Au particle sizes, being the most active among the materials tested.

1. Introduction

The production of large quantities of various chemicals and their consumption in industrial processes pose a serious threat to clean and safe drinking water, as many of these chemicals are released into the environment. Of particular concern are endocrine disrupting chemicals (EDCs), which have been shown to elicit negative effects on the endocrine system of humans and wildlife already at very low concentrations. Many of these compounds are quite stable and resistant to existing water treatment methods, so there is concern that they could enter drinking water in relatively large concentrations. One of these compounds, which have an endocrine disrupting impact if present in excessive concentrations, is coumarin, which is used in many skin care products (toilet soaps, bath oils, detergents, lotions, etc.) [1,2]. European countries have set a maximum level for coumarins of 2 mg kg^{-1} for food and 10 mg L^{-1} for alcoholic beverages [3]. Over the last decades, different processes such as advanced oxidation processes (AOPs) have been developed with the aim of eliminating pollutants that are present in water, in order to provide a solution to a real and growing problem, the scarcity of freshwater resources worldwide with not good forecasts for many countries all over the world according to World Resources Institute [4,5]. In this sense, heterogeneous photocatalysis has been developed for

* Corresponding author.
** Corresponding author at: National Institute of Chemistry, Hajdrihova 19, Ljubljana SI-1000, Slovenia.
E-mail addresses: gregor.zerjav@ki.si (G. Žerjav), natasa.novak.tusar@ki.si (N.N. Tušar).

https://doi.org/10.1016/j.cattod.2024.114764
Received 30 January 2024; Received in revised form 13 April 2024; Accepted 26 April 2024
Available online 27 April 2024

water treatment since 1973 [5], where the selected support, and sometimes also the active phase, of the catalyst is a semiconductor, such as TiO_2, ZnO, SiO_2, Fe_2O_3, CdS, ZnS [6,7].

In semiconductor photocatalysts, a band gap between the conduction band (CB) and valence band (VB) in the band structure is established. When a photon of energy higher or equal to the bandgap energy is absorbed by a semiconductor particle, an electron from the VB is promoted to the CB with simultaneous generation of a hole (h^+) in the VB [6,8,9]. The oxidative pathway could be performed by direct hole attack, where adsorbed organic molecules react with a VB hole (h^+) or indirect mode mediated by hydroxyl radicals ($OH^\bullet$), in their free or adsorbed form, that are produced after a reaction of water molecule adsorbed on the catalyst surface or with the reduction of O_2 to superoxide anion radicals ($O_2^{\bullet}$) [6,9–11].

TiO_2 is a n-type semiconductor widely used in the last decades for photocatalytic processes due to its non-toxicity, availability, versatility of applications, and effective degradation of organic pollutants [12,13]. Despite its advantages, TiO_2 also has its limitations, leading to recent research efforts focusing on improving its photocatalytic properties. [14]. One approach is the doping of TiO_2 with "impurities" of different chemical nature. Plasmonic composite materials in which titanium dioxide is doped with noble metal nanoparticles, in particular silver (Ag) and gold (Au), have attracted great interest [15]. Metallic dopants can alter the absorption properties of TiO_2-based composites through localized surface plasmon resonance (LSPR) phenomena, whereby the intensity and mode can be adjusted by varying the size, shape and amount of the dopant [16–23]. These metal nanoparticles can act as electron storage and sink for the interfacial charge transfer processes [24]. Typically, the energy of a noble metal's Fermi level is less than that of TiO_2's conduction band edge. Thus, whereas photo-produced holes stay in the semiconductor valence band, photo-promoted electrons can be collected by noble metals [24]. The position of the presence of Au surface plasmon band absorption is between 450 and 650 nm when Au is deposited onto TiO_2 [24–26]. A so called Schottky barrier originates at the metal-semiconductor interface upon light irradiation, which decelerates the charge carriers' recombination by trapping electrons and enabling their separation and utilization in redox processes [21]. The height of the Schottky barrier (SBH) can be defined as the difference between the TiO_2 conduction band and the metal Fermi level [25].

Among the metallic dopants (i.e. Au [27], Ag [28], Pt [29], Pd [30]), gold with finite nanoparticle size can spatially separate the photo-generated charge carriers and is the subject of active theoretical studies and various practical applications [31]. There are many research works that investigate the optical properties of Au/TiO_2. Žerjav et al. [32] studied the influence of different TiO_2 supports (nanoparticles (TNP) and synthesised nanorods (TNR)) on the photocatalytic activity of Au/TiO_2 composites toward the degradation of water dissolved bisphenol A (BPA). The results show that the different point of zero charge of the TiO_2 supports ($pH_{PZC} = 2.8$ for TNP and $pH_{PZC} = 7.2$ for TNR) influenced the properties of the synthesised Au/TiO_2 composites as for example the average gold particle size and consequently the catalytic activity of the studied Au/TiO_2 composites. The maximum BPA degradation rate (75 % after 120 min of reaction time under visible light illumination) was obtained with the Au/TNR composite with the average Au size of 9.4 nm and the SBH of 0.16 eV. Further Žerjav et al. [33] observed an increase in the average Au particles size from 27.1 to 54.9 nm with the increasing amount of Au in the investigated Au/TNP catalyst from 0.25 to 2.0 wt % due to the "clustering" effect during the wet impregnation synthesis procedure. The results reveal that the lowest SBH (0.15 eV) for the (2 wt %) Au/TNP led to the highest conversion of BPA (69 %) in 120 min of reaction time. Slapničar et al. [34] studied how different durations of the mixing in the impregnation of Au onto TiO_2 nanorods can affect the particle size of Au and the effect of this in the BPA degradation under visible light illumination. On the contrary, Slapničar et al. concluded that BPA oxidation grows until 40 % by raising the SBH until the maximum of 0.33 eV and decreasing the average size of Au ensembles on the surface of TiO_2 nanorods until 22.8 nm. Gomes Silva et al. [35] investigated the photocatalytic activity of Au/TiO_2 catalyst in the water splitting and demonstrated that Au loading, Au particle size, and calcination temperature were important factors in the photocatalytic activity of Au/TiO_2 materials, being the optimal catalyst containing 0.2 wt % Au with 1.87 nm average particle size and calcined at 200°C. According to Li et al. [36], fine Au nanoparticles have reduced intrinsic catalytic activity in low-temperature CO oxidation and are less able to activate surface lattice oxygen at the Au–TiO_2 perimeters than larger Au nanoparticles.

The aim of the work presented herein is to investigate how the surface charge of the TiO_2 support influences the size of the as-grown Au NPs and the photocatalytic activity of the obtained Au/TiO_2 nanorod composites. The synthesised plasmonic-based Au/TiO_2 nanocomposites were characterized in detail and the optical, electronic and photocatalytic properties investigated and determined. The photocatalytic activity in the presence of coumarin as a probe molecule under visible-light illumination and the formation of $OH^\bullet$ radicals was also monitored.

2. Experimental

2.1. Materials

Sodium hydroxide (NaOH, pellets for analysis, CAS no. 1310–73–2), and hydrochloric acid (HCl fumant 37 %, CAS no. 7647–01–0) were supplied by Supelco. Gold (III) chloride hydrate ($HAuCl_4 \cdot x\,H_2O$, ~50 % Au basis, CAS no. 27988–77–8), 2,2′-azino-bis-(3-ethylbenzothiazoline-6-sulfonic acid) cation ($ABTS^{\bullet+}$, CAS no. 30931–67–0), potassium persulfate ($K_2S_2O_8$, ≥99 %) and bisphenol A (BPA, ≥99 %, CAS no. 80–05–7) were provided by Sigma. Cumarin (98 %, CAS no. 91–64–5) was received from Alfa Aesar. All the mentioned products were used directly and unmodified in the experiments. DT-51 was the precursor for TiO_2 and was donated by Cristal Activ™. Prepared solutions in this work were prepared with ultrapure water (18.2 MΩ cm) and kept in the dark at 4ºC.

2.2. Photocatalyst synthesis

Pure anatase TiO_2 nanorods (TNR) were prepared by hydrothermal synthesis for 24 h at 130ºC in a basic medium in an autoclave reactor according to the modified method of Žerjav et al. [37] After washing several times with ultrapure water to adjust the pH from basic to neutral, the solution was first left overnight in 0.1 M HCl, repeating this procedure several times, and then, after further washes, overnight in ultrapure water, repeating this procedure twice. We prepared different supports (3 samples in total) and varied the number of washes in the intermediate steps: TNR-A (total of 33 washes), TNR-B (total of 55 washes), and TNR-C (total of 60 washes).

The deposition of the Au nanoparticles on the TNR was carried out by the excess solution impregnation method. For this purpose, the procedure proposed by Žerjav et al. was followed [32]. An amount of 0.5 g TNR was stirred with 25 mL of 1.26 mM $HAuCl_4 \cdot x\,H_2O$ aqueous solution for 20 h. The mixture was washed three times with ultrapure water. The material was dried at 110 ºC for 1 h and then at 100 ºC for 18 h. The sample was then calcined in air at 300 ºC for 2 h (heating ramp of 300 ºC/h). Different TNR supports were used to synthesis the Au/TNR catalysts: TNR-A for catalyst A (cat-A), TNR-B for catalyst B (cat-B) and TNR-C for catalyst C (cat-C).

2.3. Photocatalyst characterization

Zeta potential measurements of synthesised samples were performed with Zetasizer Ultra (MPT-3) Multi-purpose Titrator from Malvern Panalytical and ZS EXPLORER software at 25ºC with 0.1 M of sodium hydroxide (NaOH) and 0.1 M hydrochloric acid (HCl) for adjustment the pH from 2.5 to 9. The data shown in Fig. 1 are the average of three

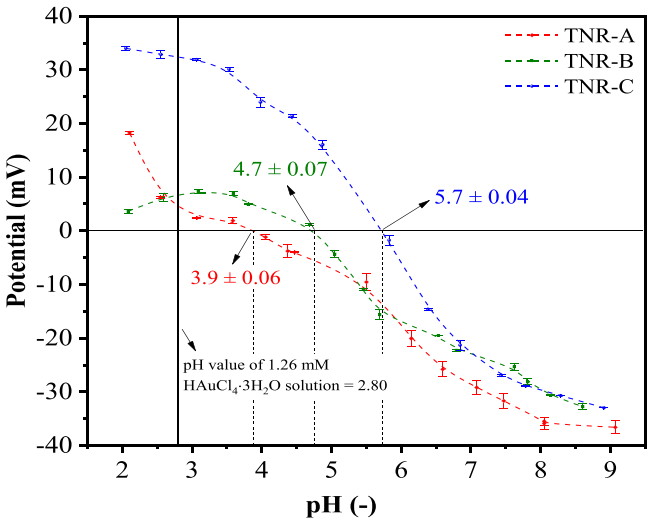

Fig. 1. Zeta potential curves as function of pH value for bare TiO_2 supports (TNR).

replicates of the zeta potential measurements for each sample analysed.

UV-Vis diffuse reflectance (UV-Vis DR) spectra were performed in a UV-Vis spectrophotometer (Perkin Elmer, Lambda 650) in the range between 200 and 900 nm with a scan speed of 266.75 nm min^{-1} with Praying Mantis™ Diffuse Reflection Accessory at room temperature.

Photoluminescence (PL) of solid samples was measured in a UV-Vis fluorescence spectrometer LS 55 of Perkin Elmer. The scan type was emission and the analysis ranged between 300 and 600 nm. The excitation wavelength was adjusted to 300 nm, the excitation and emission slit were set at 5.0 and 7.5 nm, respectively, and the scan speed was 200 nm min^{-1}. All the samples were subjected to pressure in a holder to proceed to the measurements.

The textural properties of both support and catalyst were characterized by N_2 physical adsorption-desorption in a Micromeritics TriStar II 3020 apparatus. The pretreatment of the sample was degassed with N_2 ($\geq$ 99.9999 %) at 90ºC for 60 min (10ºC min^{-1}) and 180ºC for 240 min (10ºC min^{-1}) for both support and catalyst. The specific surface area of the support and catalyst was determined by the Brunauer–Emmett–Teller (BET) and the pore size distribution of the solid materials was determined by the Barrett–Joyner–Halenda (BJH) method.

X-ray diffraction (XRD) measurements were carried out with a high-resolution X-ray powder diffractometer PANalytical X'Pert PRO MPD (PANalytical B.V., Almelo, The Netherlands) with α1 configuration ($CuK_{\alpha 1}$ $\lambda = 1.5406$ Å radiation). Diffractograms were recorded with a step size of 0.034° and an integration time of 100 s in the 2θ range from 5 to 100° using a fully open scanning X'Celerator detector for support samples. Diffractograms were recorded with a step size of 0.034° and an integration time of 3000 s in the 2θ range from 10 to 100° using a fully open scanning X'Celerator detector for catalyst samples to detect the presence of Au.

A scanning electron microscope (SEM, SUPRA 35 VP, Carl Zeiss) equipped with an energy-dispersive X-ray spectrometer (SEM-EDX, Inca 400, Oxford Instruments) operating at 15 kV and a transmission electron microscope (TEM, Probe Cs-corrected scanning transmission electron microscope Jeol ARM 200CF at accelerating voltage of 80 keV, Cold FEG, Jeol Centurio EDXS, GIF Quantum-ER DualEELS) were employed to analyze the morphology and chemical composition of the synthesised materials. Au particle size distribution and numerical density were measured using the Image-J program.

Reversed double-beam photoacoustic spectroscopy (RDB-PAS) was used to characterize the structure, especially surface structure, of photocatalysts according to the reported procedure [38,39]. A brief description of a laboratory-made RDB-PAS setup (BK1, Fig. S1) and the measurement are as follows. A laboratory-made stainless-steel photoacoustic (PA) cell (PASCL02–011 s; inner volume: ca 0.5 cm^3) equipped with a micro-electromechanical system (MEMS; SparkFun MEMS Microphone Breakout, INMP401 (ADMP401)) microphone module, a quartz-glass window transparent over the 250–1000 nm range of light and a sample holder was used. Prior to the measurement, methanol-saturated nitrogen was made to flow (ca. 30 mL min^{-1}; 10 min) through the cell containing a sample powder and then the cell was tightly sealed and thermstatted at 298 K. A light beam from a grating monochromator equipped with a 150-W xenon lamp (Bunkokeiki SM-25 Hypermonolight) and another 35-Hz intensity-modulated light beam from an LED (625 nm; Intelligent LED Solutions, RILI-ON01-RED1-SC211) were combined and introduced to the PA cell using a UV quartz combiner light guide (Moritex MWS5–1000SUV3). The PA signal from the microphone was detected by a digital lock-in amplifier (NF Corporation LI-5645) and recorded during wavelength scanning (600–300 nm; −5-nm step) of the non-modulated monochromatic light. The recorded RDB-PA spectrum was differentiated from the longer wavelength-side and calibrated to obtain energy-resolved distribution of electron traps (ERDT). The measurement conditions of the RDB-PAS setup was modified to a single 35-Hz intensity-modulated monochromatic light from SM-25 to measure PA spectra of samples. The band gap of samples was determined from an absorption-edge wavelength to estimate conduction band-bottom energy (CBB).

2.4. Photocatalytic experiments

To test the photocatalytic activity under visible-light illumination of the synthesised catalyst, 200 mg/L aqueous solution of coumarin (COUM) was employed. In this sense, it can be followed the formation rate of $OH^{\bullet}$ radicals with the production of 7-hydroxycoumarin (7-OHC), a fluorescently active compound [40,41], in the reaction of oxidation of coumarin with $OH^{\bullet}$ radicals to produce 7-OHC. A glass batch reactor of 100 mL was employed for this experiment. This reaction was performed by adding 10 mg of the synthesised catalyst into 50 mL of the COUM solution. The agitation speed was set at 400 rpm. To settle the sorption equilibrium 20 min of dark phase experiment was carried out with the suspension under agitation. In the visible light experiment with a Schott lamp model KL 2500 LED (the energy spectrum of the lamp is shown in Fig. S2) at 100 % coarse, liquid samples were collected until 4 h and filtered with a regenerated cellulose filter Chromafil RC-20/25 with a pore size of 0.2 μm. The liquid samples were measured in a UV-Vis fluorescence spectrometer LS 55 of Perkin Elmer with a wavelength excitation set at 338 nm and a scan speed of 200 nm per minute. The fluorescence signal of 7-OHC detected at 456 nm is the wavelength chosen to track the concentration of these species.

3. Results and discussion

3.1. Characterization of optical, electronic and textural properties of the materials

Fig. 1 shows the zeta potential curves as a function of pH of the investigated TNR supports. The different number of washes in the intermediate steps of TNR synthesis led to TNR supports with different points of zero charge: 3.9 ± 0.06 for TNR-A, 4.7 ± 0.07 for TNR-B and 5.7 ± 0.04 for TNR-C. The results of the N_2-physisorption analysis of the

Table 1
Results of N_2 physisorption measurements (specific surface area (S_{BET}), pore volume (V_{pore}),and pore diameter (d_{pore})).

Sample	TNR-A	TNR-B	TNR-C	cat-A	cat-B	cat-C
S_{BET} (m^2/g)	87	110	99	84	98	93
V_{pore} (cm^3/g)	0.49	0.48	0.49	0.42	0.45	0.47
d_{pore} (nm)	22.3	17.4	19.7	19.5	18.5	19.9

analysed materials are shown in Table 1 and in Fig. 2a and b. The results obtained can be interpreted that the addition of Au to the TNR supports could block some pores of the TiO_2 supports, since the specific surface areas of the Au/TNR catalysts decreased compared to the specific surface areas of the corresponding TNR supports, which is also reflected in a decrease in pore volume, which is consistent with the results previously obtained in similar work [32,33]. The porosity properties of the bare TNR and the Au/TNR catalyst were further thoroughly analyzed using nitrogen sorption. The adsorption-desorption N_2 isotherm of the analysed materials shown in Fig. 2a and b and the BJH pore size distributions shown in the insets allow us to classify the isotherm as type IV according to the IUPAC classification based on the shape of the curve and the pore size range [42]. 110 $m^2 \cdot g^{-1}$ is the S_{BET} of the bare TNR, while that of the Au/TNR catalyst is slightly lower, reaching about 98 $m^2 \cdot g^{-1}$ (Fig. 2a and b). The pore size distributions calculated with the Barrett-Joyner-Halenda (BJH) model confirm the presence of mesopores with a diameter of about 25 nm, whose volume does not change significantly with bare TNR or Au/TNR catalyst (insets in Fig. 2a and b). The X-ray diffraction patterns obtained for the materials analysed are shown in Fig. 3 and show that TiO_2 is present as an anatase polymorph in all materials produced (ICCD-00–001–0562, XPert HighScore Plus 2.2.3 database), which is not surprising given a calcination temperature of 300 °C. The two strongest peaks of this anatase are at 2θ = 25.3°, which

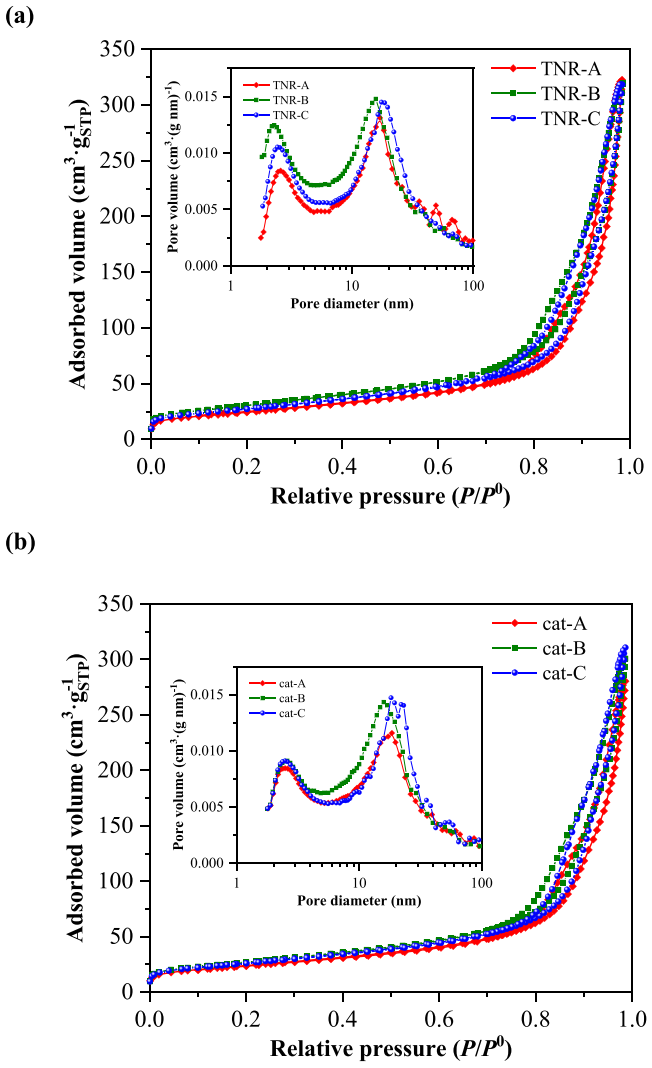

Fig. 2. Nitrogen adsorption/desorption isotherms of: (a) bare TNR supports and (b) Au/TiO_2 composites; insets show corresponding BJH pore size distribution.

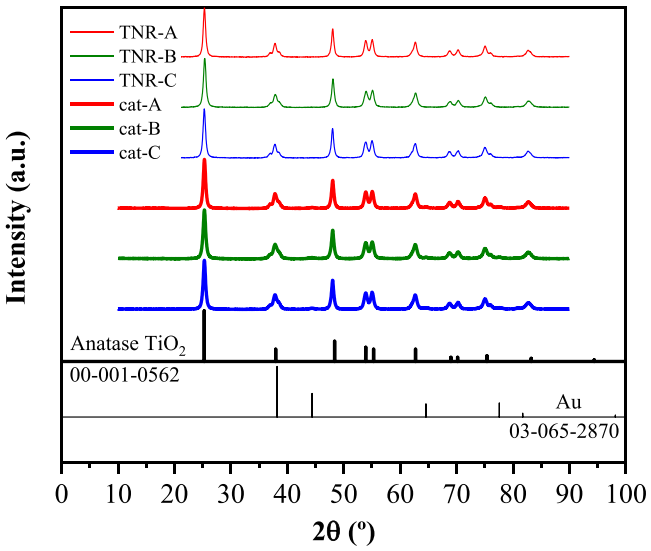

Fig. 3. XRD diffractograms of the TNR support and Au/TNR composites.

corresponds to the Miller index (1 0 1), and 2θ = 48.4° (2 0 0). The highest peak of Au (ICCD-03–065–2870) is at 2θ = 38.2°, which overlaps with the peak at 2θ = 37.9° of anatase. The apparent crystallite size of anatase TiO_2 (noting that the TNR support is not a sphere) was calculated from the diffraction peaks at the most intense anatase peak using the Scherrer equation [43], and it was found that the anatase crystallite size was the same for all materials studied, approximately 14 nm. This result can be interpreted to mean that impregnation with gold had no effect on the anatase size. The crystallite size of gold was not calculated as the most intense Au peak overlaps with the anatase peak and the remaining peaks are too small to be used for a mathematical calculation as the Au content is 1 wt % and the error of this calculation would be higher than the value obtained. The low intensity of the XRD peaks belonging to Au may also be due to the good distribution of Au particles on the surface of TNR and the small size of the Au particles [44–47].

The results of the SEM-EDX analysis (Fig. S3) of the analysed Au/TNR samples are shown in Table 2 after the mathematical treatment, where the Au loading of the catalysts is about 1.0 wt %. The Ti content is comparable to other work carried out with similar TNR supports [34]. It can be seen from Table 2 that the mean typical variation of the percentage Au content is small, indicating that the gold content is quite similar in the more than 10 areas investigated and suggesting a homogeneous distribution of gold on the surface of the TNR supports. Fig. S4 allows us to confirm the homogeneity of the distribution of the different elements by STEM-EDX elemental mapping of Ti, O and Au for the three Au/TNR samples. To further confirm the presence of gold particles, we performed additional characterization using STEM-in-SEM imaging in high-angle annular dark-field (HAADF) and bright-field (BF) modes. HAADF- and BF-STEM images of Au/TNR catalysts are presented in Fig. 4. It appears that the TNR nanoparticles have a cylindrical morphology with round ends, with a length between 20 and 40 nm and easily observable round or hemispherical Au nanoparticles. The size of the Au nanoparticles was analysed manually using the TEM images with the ImageJ programme. More than 150 Au NP were analysed in the three

Table 2
Results of the SEM-EDS elemental analysis of the investigated Au/TiO_2 composites performed at 15 kV in area scan mode at more than ten randomly selected locations.

Element (wt %)/Sample	cat-A	cat-B	cat-C
Ti	57.2 ± 0.04	56.9 ± 0.04	49.9 ± 0.04
O	41.8 ± 0.04	41.9 ± 0.04	49.2 ± 0.04
Au	0.9 ± 0.01	1.0 ± 0.01	0.9 ± 0.01

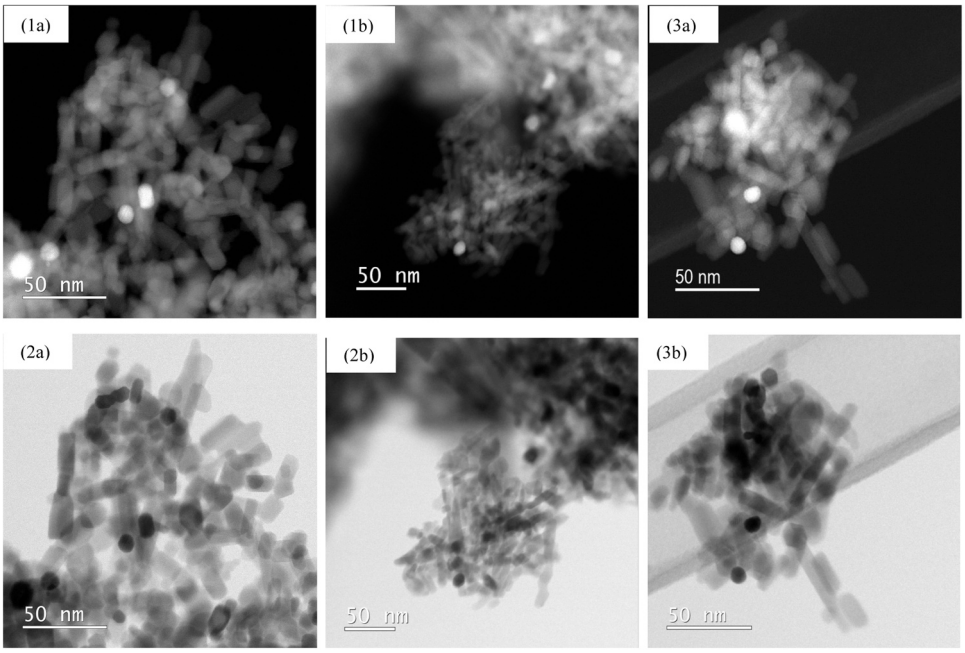

Fig. 4. STEM micrographs in (1) HAADF and (2) BF mode: (a) cat-A, (b) cat-B and (c) cat-C.

Au/TNR samples examined in order to perform an appropriate statistical analysis of the data population. The corresponding histograms of the PSD are shown in Fig. 5, where the size distribution histograms in the insets between 0 and 24 nm are magnified. The average Au particle size in the three Au/TNR samples analysed is 14.8 nm for cat-A, 12.52 nm for cat-B and 11.62 nm for cat-C. The difference between the analysed Au/TNR composites can also be evident in the size distribution of the Au particles. Cat-C has the narrowest PSD compared to cat-A, where larger Au particles are also found. Cat-B is in the middle of the two samples.

Based on the UV-Vis DR results (Fig. 6), two different light absorption ranges of the studied materials can be distinguished: The first one corresponds to the absorption below 400 nm in the UV spectra and is common for TNR supports and Au/TNR composites due to the presence of TiO_2; another range is in the 450–650 nm range due to the presence of Au NP and the LSPR effect expressed by this Au NP [36,37]. The UV-Vis DR spectra show a red shift of the maximum of the Au band and a

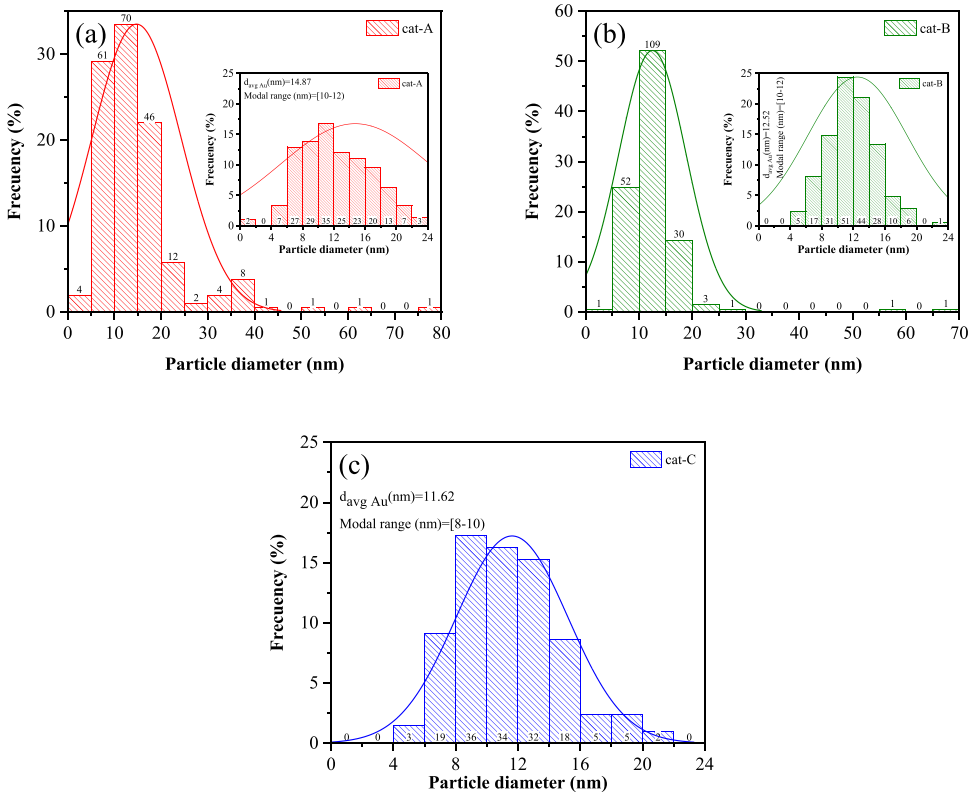

Fig. 5. Particle size distribution of Au NPs over the TNR support (insets show zoom between 0 and 24 nm): (a) cat-A, (b) cat-B and (c) cat-C.

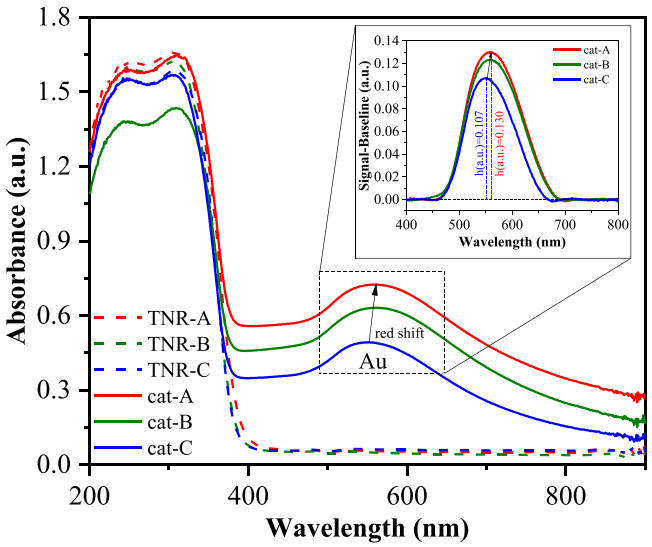

Fig. 6. UV-Vis DR spectra of the TNR support and catalysts containing 1 wt % of Au.

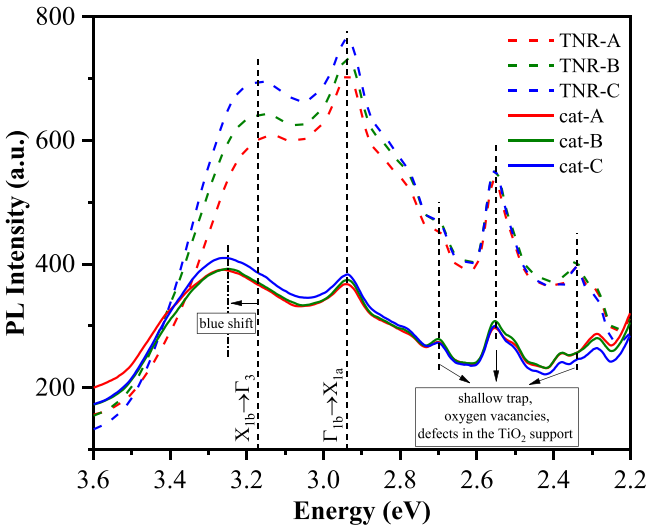

Fig. 7. Solid-state photoluminescence (PL) emission spectra of pure TiO_2 supports and Au/TiO_2 composites.

different height: higher when the pH_{PZC} of the TNR support is lower. The height was calculated using a mathematical method where a polynomial baseline was drawn for each curve and then it was possible to determine where the maximum of this area was and how high the curve was. The maximum of the curve was shifted from 552 nm for cat-C to 560 nm for cat-A, and the heights were also different: 0.107 and 0.130 a.u. respectively. The difference in the maximum absorption band in the UV-Vis DR spectra may be due to the Au content in the carrier [33,48,49], the size of the Au particles [35] and the shape of the Au NPs [33]. From these results, it can be deduced that a higher zero charge point in the carrier leads to a lower intensity in the LSPR band and a lower wavelength for the absorption maximum of the surface plasmon band (λ_{max}).

The charge carriers generated by light tend to recombine if they are not separated or utilised in an application. Therefore, the aim is to synthesise photocatalysts that have a low recombination rate of the charge carriers so that the electrons and holes can participate in the redox reactions [34]. When the charge carriers recombine, energy is released in the form of photoluminescence (PL) emissions. In this sense, a high solid-state PL signal of a material would mean a high recombination rate of the charge carriers. The results of the solid-state PL measurements of the investigated materials shown in Fig. 7 indicate that the addition of Au reduces the intensity of the PL signal compared to bare TNR, regardless of which TNR was used [32]. The peak observed at 3.17 eV is attributed to an indirect transition (X1b → Γ3) in the anatase form of the support [50,51]. A blue shift of this peak was observed in the catalyst, with the maximum of the peak shifted to 3.25 eV. This phenomenon is caused by the Au compounds in the anatase, which selectively suppress phonon-assisted indirect transitions in the support [52,53]. The lowest of these transitions observed in the PL spectra corresponds to 2.93 eV (Γ1b → X1a). The other peaks detected in the PL solid-state spectra of the investigated materials in Fig. 7 (2.34, 2.55 and 2.70 eV) are due to the presence of shallow trap levels, oxygen vacancies and defects in the TNR support, respectively, and were not affected by the presence of Au NP as they are in the same location regardless of whether it is bare TNR or Au/TNR composite material. The last important result that can be seen from Fig. 7 is the attenuation of the PL signal of the catalyst with respect to the support due to the formation of the Schottky barrier (SB) at the junction between the TiO_2 support and the Au ensemble, which acts as a sink for the visible light-generated "hot electrons" in Au and decreases the recombination rate of the carriers, thereby increasing the number of carriers available on the support surface. Fig. 7 shows that cat-C might have the highest photocatalytic activity as it has the lowest signal intensity in the range of 2.2–2.5 eV.

3.2. *Characterization of the materials by reversed double-beam photoacoustic spectroscopy (RDB-PAS)*

Fig. 8a is the ERDT (energy-resolved distribution of electron traps)/CBB (conduction-band bottom) patterns of the samples obtained by the RDB-PAS measurements, which detect the accumulation of electrons excited from the valence band to electron traps (ETs), vacant electronic level, as a function of energy from the valence-band top (VBT). ERDT is shown in reference to VBT and CBB, i.e., the energy higher than VBT by the bandgap energy is also shown in the same plot. The total density of ET, TD, is shown in < > in the unit of μmol g^{-1}.

For bare TNR samples, TNR-A, TNR-B and TNR-C, an ERDT peak appeared at ca. 3.2 eV, similar to ordinary commercial titania samples [54]. Since the RDB-PA signal intensity of those samples were higher than the ordinary samples suggesting the saturation of signal, the measurements were made for the diluted with an alumina powder (JRC-ALO-2 provided by Catalysis Society of Japan) by one fourth diluted (25 %). For the gold-loaded samples, cat-A, cat-B and cat-C, ERDT peaks were decreased below one tenth and shifted to higher-energy side. In the RDB-PAS measurements, non-modulated excitation light-wavelength was scanned from the longer-energy side, i.e., lower-energy side. Since the gold-loaded samples showed strong absorption in the wavelength range > 400 nm, i.e., visible range, the base titania could not absorb light to excite VB electrons to ETs and accumulated electrons in ETs, if any, would be transferred to gold (to evolve hydrogen) to result in lower TD and the peak shift to the higher-energy side and, therefore, the information from the ERDB/CBB patterns was limited to that appreciable part of titania particles were not in contact with gold to be able to keep electrons in their ETs.

It has been reported that, at least for titania samples, ETs detected by RDB-PAS are located predominantly on the surface, not in the bulk of particles, with area density of ca. 1 ET nm^{-1} [38,39]. The present samples also showed similar area density on the assumption that their detected ETs are also located on their surfaces, indicating that those samples are not so different from commercial titania samples and the ERDT patterns reflect their surface structure. It has been also suggested that amorphous layers, with or without in contact with crystalline layers, on the titania surfaces give ERDT peaks of energy a little higher than that of anatase or rutile-crystalline surface [54].

Fig. 8 is the result of ERDT peak-deconvolution analysis assuming

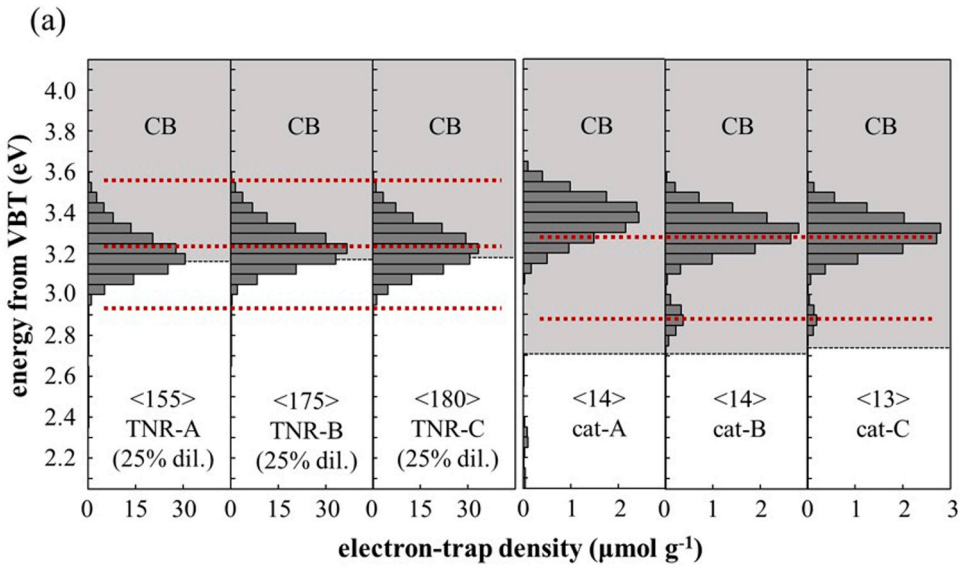

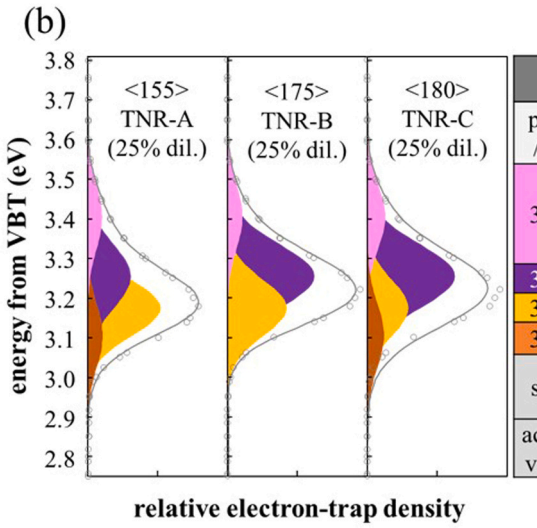

Gaussian fitting with 4 peaks				
peak /eV	TNR-A	TNR-B	TNR-C	assignment
3.40	16.4	17.0	20.2	amorphous (isolated)
3.25	49.4	100.5	101.2	amor./ana.
3.17	73.3	59.9	41.3	anatase
3.10	19.9	0.0	19.2	anatase/rutile
sum	156.0	177.4	181.8	
actual value	154.6	174.9	179.7	

Fig. 8. (a) ERDT/CBB patterns of non gold-loaded samples (TNR-A, TNR-B and TNR-C) and gold-loaded samples (cat-A, cat-B and cat-C). Total density of electron traps are shown in < > in the unit of μmol g^{-1}. (b) Peak deconvolution of ERDT patterns of the non gold-loaded samples with four Gaussian peaks at 3.10, 3.17, 3.25 and 3.40 eV.

four Gaussian peaks at 3.10, 3.17, 3.25 and 3.40 eV, assigned to anatase on rutile, anatase, amorphous in contact with anatase (amorphous on anatase) and isolated amorphous, respectively, according to the previous report [55], and clearly showed the difference in peak composition of the three samples. While the intensity of 3.40-eV isolated-amorphous and 3.10-eV anatase on rutile peak was low and not much changed for the three samples, 3.25-eV amorphous on anatase peak and 3.17-eV anatase peak were increased and decreased, respectively, in the order of TNR-A < TNR-B < TNR-C. Since CBB position, reflecting bulk structure, of those samples were almost the same, bulk anatase structure was not changed by the synthesis procedure, but the surface anatase layer was amorphized by the procedure depending on the number of washing processes. Such suggested difference in the surface structure might be related to the difference in the point of zero charge (3.9 ± 0.06 for TNR-A, 4.7 ± 0.07 for TNR-B and 5.7 ± 0.04 for TNR-C) as described in the preceding section. The origin of the amorphous TiO_2 phase in the analysed TNR samples can be explained by the results of our previous study [56], in which we showed that the TiO_2 nanorods obtained after hydrothermal treatment and washing treatment have a core–shell structure, in which the core consists of crystalline anatase TiO_2 and the shell of amorphous TiO_2. This amorphous shell is further converted into anatase TiO_2 by the final calcination step, which also led to a reduction in the specific surface area of the calcined TiO_2 nanorods compared to the non-calcined ones.

As was reported in the previous paper [55], a little lower energy-side shift, in reference to VBT, of the peak of amorphous on anatase (3.25 eV) compared to isolated-amorphous peak (3.40) is due to interparticle charge-transfer excitation of electrons from VB of anatase to amorphous ETs [57] assuming the VBT of amorphous is a little lower than that of anatase; the actual energy of amorphous on anatase is same as that or isolated amorphous, which is a little higher than the actual energy of anatase [57] and therefore it is suggested that the density of a little higher-energy vacant electronic states (ETs) is increased in the order of TNR-A < TNR-B < TNR-C, as is discussed in the following section.

If we briefly summarise the results of the measurements carried out on the tested materials to characterise their optical, textural and electronic properties, we can conclude the following: i) the number of washes after the hydrothermal synthesis of the TNR influences the zeta potential of the obtained TNR by varying the amount of surface amorphous TiO_2 layer remaining in the TNR after the calcination step, ii) an acidic pH of the TNR points of the zero charge resulted in the formation of larger Au particles, a broader Au PSD and a higher absorption and

λ_{max} intensity in the LSPR region of the UV-Vis-DR spectra, iii) while the highest pH of the TNR points of the zero charge resulted in the formation of smaller Au NPs and a narrower Au PSD and a lower absorption and λ_{max} intensity in the LSPR region of the UV-Vis DR spectra. From the study of the PSD of the Au NPs, we can confirm that the different points of zero charge in the TiO_2 support influence the nucleation of the Au NPs and this directly affects the extent of hydrolysis of the metallic precursor and its subsequent nucleation [58]. Isono et al. [59] already explained the phenomena caused by the formation of a complex between the hydroxyl groups of the TiO_2 surface and the Au(III) ions. The hydroxyl groups on the surface of TiO_2 (TiO_s-OH) have two zwitterionic forms: They can be protonated (Ti_s-OH_2^+) when the pH is lower than the pH_{PZC} of the support, or deprotonated (Ti_s-O^-) when the pH is higher than the pH_{PZC} of the support. In our case, the pH of the $HAuCl_4 \cdot x\ H_2O$ solution was 2.8 (Fig. 1), so the concentration pH of all solutions during the impregnation step is lower than the pH_{PZC} of all TNR carriers, including the acidic ones. Therefore, the protonated form of the hydroxyl groups on the surface of TiO_2 (Ti_s-OH_2^+) is available for the reaction. On the other hand, $[AuCl_4]^-$ is formed from the precursor used when it is dissolved in water. A higher nucleation rate occurs at a higher driving force, which in our case means that the highest nucleation rate is expressed by the TNR-C, as it expresses the largest difference between the pH of the gold precursor solution (2.8) and the pH of the point of zero charge. A higher nucleation rate leads to the formation of a higher number of nuclei, which in our case, where we have the same amount of gold precursor all the time, leads to the formation of Au NP with smaller size. The increase in signal intensity in the UV-is DR spectra with increasing average Au particle size is consistent with the results of other researchers [60,61].

3.3. Characterization of photocatalytic properties of the catalysts

The results of the coumarin oxidation experiments carried out under illumination with visible light in the presence of the investigated Au/TNR materials are shown in Fig. 9. For the photocatalytic experiments with the coumarin compound, it was necessary to establish a calibration curve, shown in Fig. S5, where the intensity of the fluorescence is plotted against the 7-OHC concentration. The results in Fig. 9 confirm that the all three Au/TNR catalysts can generate OH• radicals under illumination with visible light. It can be seen that cat-C with the smallest Au particle size produces the largest amount of hydroxyl radicals. According to Rayalu et al. [62], this can be explained by the fact that Au with smaller particle size could act as a co-catalyst/electron buffer and provide an active site for the formation of hydroxyl radicals under UV-Vis illumination, while the larger Au particles could act as light collectors. Considering the influence of surface structure of non gold-loaded TNR as discussed in the preceding section, the photocatalytic activity of gold-loaded TNR was also related to the surface electronic states, i.e., electron traps, as a site of transfer of photoexcited electrons to the surface-adsorbed of oxygen, a counter reaction of oxidation by positive holes; as one of possible explanation of photocatalytic activity trend, TNR-A < TNR-B < TNR-C, was caused by the increase in the surface density of a little higher-energy ETs on the surface enabling facile electron transfer during the photocatalytic reaction.

4. Conclusions

The influence of the surface charge of the TiO_2 supports onto the properties of Au/TiO_2 composites has been investigated by synthesis of TiO_2 nanorod (TNR) support with different zeta potentials by varying the numbers of washing steps during the hydrothermal synthesis of the TNR. The results shows that by varying of the numbers of the washing steps TNR supports with different points of zero charge were obtained: 3.9 ± 0.06 for TNR-A, 4.7 ± 0.07 for TNR-B and 5.7 ± 0.04 for TNR-C. The results of the RDB-PAS analysis of the investigated materials revealed that the differences in the zeta potentials of the TNR results from the different amounts of the amorphous TiO_2 which covers the anatase TiO_2 core. The obtained TNR supports were used to synthesise Au/TNR composites by a wet impregnation synthesis procedure where the pH value of the aqueous gold precursor solution was 2.8. These resulted in the synthesis of Au/TNR composites where the acidic pH value of the TNR points of the zero charge outcame in the formation of larger Au particles (dAu(cat-A)= 14.8 nm), a broader Au PSD and a higher absorption and λ_{max} intensity in the LSPR region of the UV-Vis DR spectra, while the highest pH of the TNR points of the zero charge ended in the formation of smaller Au NPs (dAu(cat-C)= 11.6 nm) and a narrower Au PSD and a lower absorption and λ_{max} intensity in the LSPR region of the UV-Vis DR spectra. The results of the coumarin oxidation experiments carried out under illumination with visible light in the presence of the investigated Au/TNR materials confirm that the three Au/TNR catalysts can generate OH• radicals under visible light illumination and that the cat-C with the smallest Au particle size produces the largest amount of hydroxyl radicals as small Au NP can act as a co-catalyst/electron buffer and provide an active site for the formation of hydroxyl radicals under UV-Vis illumination, while the larger Au NP act as light collectors. The results of the study presented here confirm that the number of washes in the intermediate steps of TNR synthesis leads to the synthesis of TNRs with different surface charges, which is due to the presence of a different amount of amorphous phase on the TNR surface and consequently leads to different average particle sizes of Au NPs in the investigated Au/TiO_2 composites synthesised by wet impregnation.

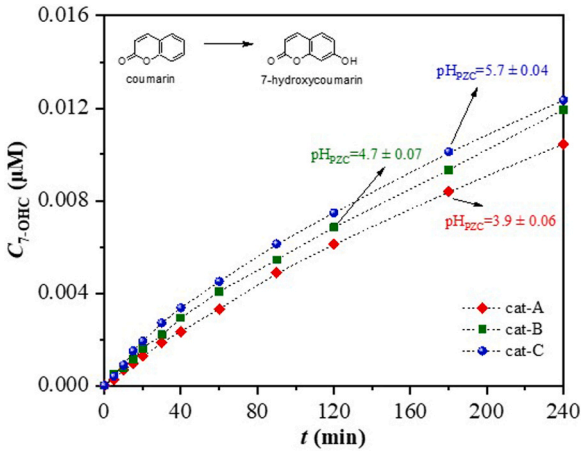

Fig. 9. 7-hydroxycoumarin concentration (7-OHC)) vs reaction time for the investigated Au/TiO_2 composites.

CRediT authorship contribution statement

Estrella Sera Perez: Investigation, Visualization, Formal analysis, Writing – original draft. **Goran Dražić:** Formal analysis, Writing – original draft. **Mai Takashima** and **Bunsho Ohtani:** Formal analysis, Writing – original draft. **Sebastijan Kovačič:** Supervision, Methodology, Writing - review & editing. **Gregor Žerjav:** Conceptualization, Methodology, Writing - review & editing. **Nataša Novak Tušar:** Supervision, Writing - review & editing, Project administration, Funding acquisition.

Declaration of Competing Interest

The authors declare that they have no known competing financial interests or personal relationships that could have appeared to influence the work reported in this paper.

Data Availability

Data will be made available on request.

Acknowledgements

The authors gratefully acknowledge the financial support from the European Social Fund provided through the Margarita Salas contract from Spain, and the Slovenian Research and Innovation Agency (research programs P1–0418 and P2–0150) and NETPORE COST action CA20126.

Appendix A. Supporting information

Supplementary data associated with this article can be found in the online version at doi:10.1016/j.cattod.2024.114764.

References

[1] M. Blanco, J. Rizzi, D. Fernandes, N. Colin, A. Maceda-Veiga, C. Porte, Assessing the impact of waste water effluents on native fish species from a semi-arid region, NE Spain, Sci. Total Environ. 654 (2019) 218–225, https://doi.org/10.1016/j.scitotenv.2018.11.115.

[2] Ö. Görmez, S. Akay, B. Gözmen, B. Kayan, D. Kalderis, Degradation of emerging contaminant coumarin based on anodic oxidation, electro-Fenton and subcritical water oxidation processes, Environ. Res 208 (2022) 112736, https://doi.org/10.1016/j.envres.2022.112736.

[3] M. Lončar, M. Jakovljević, D. Šubarić, M. Pavlić, V. Buzjak Služek, I. Cindrić, M. Molnar, Coumarins in food and methods of their determination, Foods 9 (2020) 645.

[4] A. Maddocks, R.S. Young, P. Reig, Ranking the world's most water-stressed countries in 2040, World Resource Institute (WRI) (2015). ⟨https://www.wri.org/blog/2015/08/ranking-world-s-most-water-stressed-countries-2040⟩ (accessed November 9, 2023).

[5] B. Ohtani, M. Takashima, Happy photocatalysts and unhappy photocatalysts: electron trap-distribution analysis for metal oxide-sample identification, Catal. Sci. Technol. 12 (2022) 354–359.

[6] A.G. Akerdi, S.H. Bahrami, Application of heterogeneous nano-semiconductors for photocatalytic advanced oxidation of organic compounds: a review, J. Environ. Chem. Eng. 7 (2019) 103283.

[7] S.T. Nishanthi, Visible light photocatalytic degradation of environmental pollutants using metal oxide semiconductors, : Photo Funct. Mater. Environ. Remediat. (2019) 41–67, https://doi.org/10.1002/9781119529941.ch2.

[8] K. Wetchakun, N. Wetchakun, S. Sakulsermsuk, An overview of solar/visible light-driven heterogeneous photocatalysis for water purification: TiO_2- and ZnO-based photocatalysts used in suspension photoreactors, J. Ind. Eng. Chem. 71 (2019) 19–49.

[9] M.I. Litter, Heterogeneous photocatalysis: transition metal ions in photocatalytic systems, Appl. Catal. B 23 (1999) 89–114.

[10] J. Zhong, Y. Zhao, L. Ding, H. Ji, W. Ma, C. Chen, J. Zhao, Opposite photocatalytic oxidation behaviors of BiOCl and TiO_2: direct hole transfer vs. indirect OH oxidation, Appl. Catal. B 241 (2019) 514–520, https://doi.org/10.1016/j.apcatb.2018.09.058.

[11] Z. Rao, G. Lu, L. Chen, A. Mahmood, G. Shi, Z. Tang, X. Xie, J. Sun, Photocatalytic oxidation mechanism of Gas-Phase VOCs: unveiling the role of holes, •OH and •O2−, Chem. Eng. J. 430 (2022) 132766 https://doi.org/10.1016/j.cej.2021.132766.

[12] J. Liu, X. Sun, Y. Fan, Y. Yu, Q. Li, J. Zhou, H. Gu, K. Shi, B. Jiang, P-N heterojunction embedded CuS/TiO_2 bifunctional photocatalyst for synchronous hydrogen production and benzylamine conversion, Small (2023) 2306344, https://doi.org/10.1002/smll.202306344.

[13] V.C. Anitha, A.N. Banerjee, S.W. Joo, Recent developments in TiO_2 as n- and p-type transparent semiconductors: synthesis, modification, properties, and energy-related applications, J. Mater. Sci. 50 (2015) 7495–7536, https://doi.org/10.1007/s10853-015-9303-7.

[14] C. Liu, C. Xu, W. Wang, L. Chen, X. Li, Y. Wu, Oxygen vacancy mediated band-gap engineering via B-doping for enhancing Z-scheme A-TiO_2/R-TiO_2 heterojunction photocatalytic performance, Nanomaterials 13 (2023) 794.

[15] M. Dahl, Y. Liu, Y. Yin, Composite titanium dioxide nanomaterials, Chem. Rev. 114 (2014) 9853–9889.

[16] A. Orlov, D.A. Jefferson, M. Tikhov, R.M. Lambert, Enhancement of MTBE photocatalytic degradation by modification of TiO_2 with gold nanoparticles, Catal. Commun. 8 (2007) 821–824, https://doi.org/10.1016/j.catcom.2006.08.040.

[17] E. Kowalska, R. Abe, B. Ohtani, Visible light-induced photocatalytic reaction of gold-modified titanium(IV) oxide particles: action spectrum analysis, Chem. Commun. (2009) 241–243. ⟨https://www.scopus.com/inward/record.uri?eid=2-s2.0-58049202885&doi=10.1039%2fb815679d&partnerID=40&md5=0aeaf83336abdb2eb4f3248b9d92fb46⟩.

[18] L. Lin, Q. Zhong, Y. Zheng, Y. Cheng, R. Qi, R. Huang, Size effect of Au nanoparticles in Au-TiO_2-x photocatalyst, Chem. Phys. Lett. 770 (2021) 138457, https://doi.org/10.1016/j.cplett.2021.138457.

[19] R.S. Sonawane, M.K. Dongare, Sol–gel synthesis of Au/TiO_2 thin films for photocatalytic degradation of phenol in sunlight, J. Mol. Catal. A Chem. 243 (2006) 68–76, https://doi.org/10.1016/j.molcata.2005.07.043.

[20] P. Wang, B. Huang, Y. Dai, M.-H. Whangbo, Plasmonic photocatalysts: harvesting visible light with noble metal nanoparticles, Phys. Chem. Chem. Phys. 14 (2012) 9813–9825.

[21] I. Wysocka, E. Kowalska, J. Ryl, G. Nowaczyk, A. Zielińska-Jurek, Morphology, photocatalytic and antimicrobial properties of TiO_2 modified with mono-and bimetallic copper, platinum and silver nanoparticles, Nanomaterials 9 (2019) 1129.

[22] W.A. Murray, W.L. Barnes, Plasmonic materials, Adv. Mater. 19 (2007) 3771–3782.

[23] L. Brus, Noble metal nanocrystals: plasmon electron transfer photochemistry and single-molecule Raman spectroscopy, Acc. Chem. Res. 41 (2008) 1742–1749.

[24] G.M. Veith, A.R. Lupini, N.J. Dudney, Role of pH in the formation of structurally stable and catalytically active TiO_2-supported gold catalysts, J. Phys. Chem. C 113 (2009) 269–280.

[25] A. Zielińska-Jurek, Progress, challenge, and perspective of bimetallic TiO_2-based photocatalysts, J. Nanomater 2014 (2014) 3.

[26] H. Zhu, X. Yuan, Q. Yao, J. Xie, Shining photocatalysis by gold-based nanomaterials, Nano Energy 88 (2021) 106306.

[27] N. Kunthakudee, P. Ramakul, K. Serivalsatit, M. Hunsom, Photosynthesis of Au/TiO_2 nanoparticles for photocatalytic gold recovery from industrial gold-cyanide plating wastewater, Sci. Rep. 12 (2022) 21956, https://doi.org/10.1038/s41598-022-24290-7.

[28] D. Kanakaraju, F.D. anak Kutiang, Y.C. Lim, P.S. Goh, Recent progress of Ag/TiO_2 photocatalyst for wastewater treatment: doping, co-doping, and green materials functionalization, Appl. Mater. Today 27 (2022) 101500, https://doi.org/10.1016/j.apmt.2022.101500.

[29] G. Žerjav, Z. Say, J. Zavašnik, M. Finšgar, C. Langhammer, A. Pintar, Photo, thermal and photothermal activity of TiO_2 supported Pt catalysts for plasmon-driven environmental applications, J. Environ. Chem. Eng. 11 (2023) 110209, https://doi.org/10.1016/j.jece.2023.110209.

[30] Y. Chen, L. Soler, M. Armengol-Profitós, C. Xie, D. Crespo, J. Llorca, Enhanced photoproduction of hydrogen on Pd/TiO_2 prepared by mechanochemistry, Appl. Catal. B 309 (2022) 121275, https://doi.org/10.1016/j.apcatb.2022.121275.

[31] A. Ayati, A. Ahmadpour, F.F. Bamoharram, B. Tanhaei, M. Mänttäri, M. Sillanpää, A review on catalytic applications of Au/TiO_2 nanoparticles in the removal of water pollutant, Chemosphere 107 (2014) 163–174, https://doi.org/10.1016/j.chemosphere.2014.01.040.

[32] G. Žerjav, J. Zavašnik, J. Kovač, A. Pintar, The influence of Schottky barrier height onto visible-light triggered photocatalytic activity of TiO_2 + Au composites, Appl. Surf. Sci. 543 (2021), https://doi.org/10.1016/j.apsusc.2020.148799.

[33] G. Žerjav, M. Roškarič, J. Zavašnik, J. Kovač, A. Pintar, Effect of Au loading on Schottky barrier height in TiO_2 + Au plasmonic photocatalysts, Appl. Surf. Sci. 579 (2022), https://doi.org/10.1016/j.apsusc.2021.152196.

[34] S. Slapničar, G. Žerjav, J. Zavašnik, M. Finšgar, A. Pintar, Synthesis and characterization of plasmonic Au/TiO_2 nanorod solids for heterogeneous photocatalysis, J. Environ. Chem. Eng. 11 (2023), https://doi.org/10.1016/j.jece.2023.109835.

[35] C. Gomes Silva, R. Juárez, T. Marino, R. Molinari, H. García, Influence of excitation wavelength (UV or visible light) on the photocatalytic activity of titania containing gold nanoparticles for the generation of hydrogen or oxygen from water, J. Am. Chem. Soc. 133 (2011) 595–602.

[36] D. Li, R. You, M. Yang, Y. Liu, K. Qian, S. Chen, T. Cao, Z. Zhang, J. Tian, W. Huang, Morphology-dependent evolutions of sizes, structures, and catalytic activity of Au nanoparticles on anatase TiO_2 nanocrystals, J. Phys. Chem. C 123 (2019) 10367–10376.

[37] G. Žerjav, M.S. Arshad, P. Djinović, I. Junkar, J. Kovač, J. Zavašnik, A. Pintar, Improved electron-hole separation and migration in anatase TiO_2 nanorod/reduced graphene oxide composites and their influence on photocatalytic performance, Nanoscale 9 (2017) 4578–4592, https://doi.org/10.1039/c7nr00704c.

[38] A. Nitta, M. Takase, M. Takashima, N. Murakami, B. Ohtani, A fingerprint of metal-oxide powders: Energy-resolved distribution of electron traps, Chem. Commun. 52 (2016) 12096–12099.

[39] A. Nitta, M. Takashima, N. Murakami, M. Takase, B. Ohtani, Reversed double-beam photoacoustic spectroscopy of metal-oxide powders for estimation of their energy-resolved distribution of electron traps and electronic-band structure, Electro Acta 264 (2018) 83–90.

[40] G. Žerjav, A. Albreht, I. Vovk, A. Pintar, Revisiting terephthalic acid and coumarin as probes for photoluminescent determination of hydroxyl radical formation rate in heterogeneous photocatalysis, Appl. Catal. A Gen. 598 (2020) 117566, https://doi.org/10.1016/j.apcata.2020.117566.

[41] G. Louit, S. Foley, J. Cabillic, H. Coffigny, F. Taran, A. Valleix, J.P. Renault, S. Pin, The reaction of coumarin with the OH radical revisited: hydroxylation product analysis determined by fluorescence and chromatography, Radiat. Phys. Chem. 72 (2005) 119–124, https://doi.org/10.1016/j.radphyschem.2004.09.007.

[42] F.J. Sotomayor, K.A. Cychosz, M. Thommes, Characterization of micro/mesoporous materials by physisorption: concepts and case studies, Acc. Mater. Surf. Res. 3 (2018) 34–50.

[43] W.-T. Chen, A. Chan, Z.H.N. Al-Azri, A.G. Dosado, M.A. Nadeem, D. Sun-Waterhouse, H. Idriss, G.I.N. Waterhouse, Effect of TiO_2 polymorph and alcohol sacrificial agent on the activity of Au/TiO_2 photocatalysts for H2 production in alcohol–water mixtures, J. Catal. 329 (2015) 499–513, https://doi.org/10.1016/j.jcat.2015.06.014.

[44] B. Cojocaru, V. Andrei, M. Tudorache, F. Lin, C. Cadigan, R. Richards, V. I. Parvulescu, Enhanced photo-degradation of bisphenol pollutants onto gold-modified photocatalysts, Catal. Today 284 (2017) 153–159.

[45] D. Shi, J. Liu, S. Ji, Preparation of Au/TiO_2 catalyst and the performance of liquid methanol catalytic oxidation to formic acid, Ind. Eng. Chem. Res. 56 (2017) 11028–11033.
[46] M. Alvaro, B. Cojocaru, A.A. Ismail, N. Petrea, B. Ferrer, F.A. Harraz, V. I. Parvulescu, H. Garcia, Visible-light photocatalytic activity of gold nanoparticles supported on template-synthesized mesoporous titania for the decontamination of the chemical warfare agent Soman, Appl. Catal. B 99 (2010) 191–197.
[47] M. Mrowetz, A. Villa, L. Prati, E. Selli, Effects of Au nanoparticles on TiO_2 in the photocatalytic degradation of an azo dye, Gold. Bull. 40 (2007) 154–160.
[48] Z. Zheng, B. Huang, X. Qin, X. Zhang, Y. Dai, M.H. Whangbo, Facile in situ synthesis of visible-light plasmonic photocatalysts M@TiO_2 (M = Au, Pt, Ag) and evaluation of their photocatalytic oxidation of benzene to phenol, J. Mater. Chem. 21 (2011) 9079–9087, https://doi.org/10.1039/c1jm10983a.
[49] Y. Ma, K. Kobayashi, Y. Cao, T. Ohno, Development of visible-light-responsive morphology-controlled brookite TiO_2 nanorods by site-selective loading of AuAg bimetallic nanoparticles, Appl. Catal. B 245 (2019) 681–690, https://doi.org/10.1016/j.apcatb.2019.01.016.
[50] V. Jovic, Z.H.N. Al-Azri, W.-T. Chen, D. Sun-Waterhouse, H. Idriss, G.I. N. Waterhouse, Photocatalytic H2 production from ethanol–water mixtures over Pt/TiO_2 and Au/TiO_2 photocatalysts: a comparative study, Top. Catal. 56 (2013) 1139–1151.
[51] N. Serpone, D. Lawless, R. Khairutdinov, Size effects on the photophysical properties of colloidal anatase TiO_2 particles: size quantization versus direct transitions in this indirect semiconductor? J. Phys. Chem. 99 (1995) 16646–16654, https://doi.org/10.1021/j100045a026.
[52] H. Nakajima, T. Mori, M. Watanabe, Influence of platinum loading on photoluminescence of TiO_2 powder, J. Appl. Phys. 96 (2004) 925–927.
[53] H. Nakajima, T. Mori, Photoluminescence of Pt-loaded TiO_2 powder, Phys. B Condens Matter 376–377 (2006) 820–822, https://doi.org/10.1016/j.physb.2005.12.205.
[54] A. Nitta, M. Takashima, M. Takase, B. Ohtani, Identification and characterization of titania photocatalyst powders using their energy-resolved distribution of electron traps as a fingerprint, Catal. Today 321 (2019) 2–8.
[55] G. Chen, M. Takashima, B. Ohtani, Direct amorphous-structure analysis: How are surface/bulk structure and activity of titania photocatalyst particles changed by milling? Chem. Lett. 50 (2021) 644–648.
[56] G. Žerjav, M.S. Arshad, P. Djinović, I. Junkar, J. Kovač, J. Zavašnik, A. Pintar, Improved electron–hole separation and migration in anatase TiO_2 nanorod/reduced graphene oxide composites and their influence on photocatalytic performance, Nanoscale 9 (2017) 4578–4592.
[57] Y. Shen, A. Nitta, M. Takashima, B. Ohtani, Do particles interact electronically?—proof of interparticle charge-transfer excitation between adjoined anatase and rutile particles, Chem. Lett. 50 (2021) 80–83.
[58] C. Rodríguez-Martínez, Á.E. García-Domínguez, F. Guerrero-Robles, R.O. Saavedra-Díaz, G. Torres-Torres, C. Felipe, R. Ojeda-López, A. Silahua-Pavón, A. Cervantes-Uribe, Synthesis of supported metal nanoparticles (Au/TiO_2) by the suspension impregnation method, J. Compos. Sci. 4 (2020) 89.
[59] R. Isono, T. Yoshimura, K. Esumi, Preparation of Au/TiO_2 nanocomposites and their catalytic activity for DPPH radical scavenging reaction, J. Colloid Interface Sci. 288 (2005) 177–183, https://doi.org/10.1016/j.jcis.2005.02.078.
[60] P.K. Jain, K.S. Lee, I.H. El-Sayed, M.A. El-Sayed, Calculated absorption and scattering properties of gold nanoparticles of different size, shape, and composition: applications in biological imaging and biomedicine, J. Phys. Chem. B 110 (2006) 7238–7248.
[61] A.R. Shafiqa, A. Abdul Aziz, B. Mehrdel, Nanoparticle optical properties: size dependence of a single gold spherical nanoparticle. J. Phys. Conf. Ser., IOP Publishing, 2018 012040.
[62] S.S. Rayalu, D. Jose, M.V. Joshi, P.A. Mangrulkar, K. Shrestha, K. Klabunde, Photocatalytic water splitting on Au/TiO_2 nanocomposites synthesized through various routes: enhancement in photocatalytic activity due to SPR effect, Appl. Catal. B 142–143 (2013) 684–693, https://doi.org/10.1016/j.apcatb.2013.05.057.